




Significant enhancement of electrical conductivity by incorporating carbon fiber into CoSb₃ thermoelectric skutterudite fabricated by spark plasma sintering method

Ridwone Hossain¹, Al Jumlat Ahmed¹, Frank. F. Yun¹, Lina Sang¹, Sheik Md Kazi Nazrul Islam¹, Guangsai Yang¹, Michael B. Cortie², and Xiaolin Wang^{1,*} 

¹Institute for Semiconducting & Electronic Materials, Australian Institute for Innovative Materials, University of Wollongong, Wollongong, Australia

²School of Mathematical and Physical Sciences, University of Technology Sydney, Broadway, NSW 2007, Australia

Received: 27 June 2021

Accepted: 4 October 2021

Published online:
15 October 2021

© The Author(s), under exclusive licence to Springer Science+Business Media, LLC, part of Springer Nature 2021

ABSTRACT

The effects of carbon fiber additions on the electrical and thermoelectric performance in *p*-type CoSb₃-based skutterudite are reported. A threefold enhancement in electrical conductivity is found. Two different explanations for the increased electrical conductivity are considered: Either carbon atoms enter the CoSb₃ lattice as a dopant that makes it more and more conductive, or the increase in conductivity is due to electrical percolation of the carbon fibers in the composite. X-ray diffraction data show that the lattice parameter of the CoSb₃ is not affected by the presence of the carbon fiber; however, adding carbon is associated with precipitation of 20 wt. % elemental Sb. DFT calculations show that the enthalpy of formation of a solid solution of carbon (interstitial or as a substitution for Sb) is slightly positive. This would be offset by an increased entropy contribution at higher temperatures, so the free energy change overall is likely to be favorable. All of the results support an explanation based on an improved electrical conductivity of a very dilute solid solution of C in CoSb₃. The average thermoelectric parameters of the composite material, including heat conductivity, average composite Seebeck coefficient, Hall effect, carrier mobility, and carrier concentration, were influenced by the carbon addition. Unfortunately, the effects largely cancel each other so that the overall *zT* of the composite was not improved.

Handling Editor: P. Nash.

Address correspondence to E-mail: xiaolin@uow.edu.au

Introduction

Thermoelectric materials have the excellent property of producing electricity from heat. Their availability has enabled the manufacture of thermoelectric generators which have no moving parts or working fluids and which require negligible maintenance [1–4]. Thermoelectric technology has also expanded its use in applications such as recovering energy from waste heat from chimneys [5, 6], exhausted heat after a heat engine produces the necessary power to drive any vehicle or generator [7–11], and conversion of abundant solar irradiance to electricity (the latter by incorporation into solar thermal or solar thermal photovoltaic systems), among other applications [12–14]. Thermoelectric materials are now widely recognized as promising energy materials, with a great deal of research and effort now focused on optimizing their physical characteristics along with finding the best candidate material for numerous energy applications.

A dimensionless figure of merit (zT) is a common benchmark for improved energy conversion efficiency of thermoelectric materials, where zT is a figure of merit defined by the following equation: $zT = \left(\frac{S^2\sigma}{k}\right)T$. In the above equation, S, σ, k , and T are the Seebeck coefficient, electrical conductivity, thermal conductivity, and absolute temperature, respectively. In fact, power factor is essentially a function of electrical conductivity and the Seebeck coefficient ($PF = S^2\sigma$). The figure of merit is the determining factor for any thermoelectric material that indicates how superior the material is at some given operating temperature, with different superiority ranges for different materials. To obtain a high zT , high electrical conductivity, a high Seebeck coefficient, and low thermal conductivity are required.

CoSb₃-based skutterudites are one of the more promising thermoelectric materials for intermediate temperature applications because they contain octahedral void space that can accommodate filler atoms and these could contribute to lower phonon vibrations in the lattice [15]. There have been several successful attempts to insert filler atoms into the voids of skutterudites with the intention of lowering

the phonon wavelength to bring about a better zT . These atoms are known as ‘rattlers’ because they can move around in the void [16]. For example, *n*-type CoSb₃ has been doped with Ga and Yb, where Ga was substituted on Sb sites while also occupying the void sites, and increasing Yb content facilitated improved Seebeck voltage and effective mass [17]. In another attempt, In (indium) was inserted into the voids of CoSb₃, which reduced lattice thermal conductivity without harming the power factor, whereas a slight amount of Ga substituted for Sb provided a zT of 0.9 [18]. In other work, several elements of group IVB were simultaneously doped into CoSb₃ to observe which of the elements could fill the voids, and Sn was found to be the most effective element to decrease the thermal conductivity [19]. The use of an optimum fraction of In as a fourth filler has been investigated together with the influences of microstructure, crystallite size, and thermal stability, and ways found to provide reduced thermal conductivity [20]. These types of filled CoSb₃ were mixed with magnetic nanoparticles at a later stage to prepare a series of magnetic nanocomposite thermoelectric materials, where significant suppression of lattice thermal conductivity was obtained by introducing paramagnetism [21, 22].

While it is well established that thermal conductivity in skutterudites can be reduced by using filler atoms, it is important not to ignore other means by which the thermoelectric properties may be improved. If the properties can be first improved without using rattlers, then additional improvement should follow when rattlers are included later [23].

In the present work, we show how a threefold enhancement of electrical conductivity over a temperature range from 300 to 700 K can be achieved by incorporating a small amount of carbon fiber (CF) in *p*-type CoSb₃. To our knowledge, there has been no published work in the literature so far that reports such a large enhancement of electrical conductivity by incorporating carbon fiber in *p*-type CoSb₃ composite. Various high electrical conductivity profiles for different proportions of carbon fiber inclusion are demonstrated in this work. All the thermoelectric parameters were influenced by the carbon addition, although the overall zT was not significantly affected.

Methods

Computational details

First, first-principle calculations were performed using density functional theory (DFT) implemented using the CASTEP package [24]. The exchange–correlation function used to describe the exchange–correlation interaction was the general gradient approximation (GGA) with the Perdew–Burke–Ernzerhof (PBE) formulation [25]. Structures are optimized using the Broyden–Fletcher–Goldfarb–Shanno (BFGS) algorithm [26]. The relevant doping is made as shown in the figures. The maximum cutoff energy was set at 420 eV with a $2 \times 2 \times 2$ k point set for optimizations with an ultrasoft pseudopotential; for the DOS, the calculations were performed with a $16 \times 16 \times 16$ k point mesh. Lattice relaxation has been performed for the primitive cell for each doping case by minimizing energies to less than 5×10^{-6} eV/atom. Enthalpy of formation of the pure CoSb₃ is with reference to the pure elements in their standard states at 0 K, whereas for the defective structures it is with reference to the pure CoSb₃ and the pure elements additionally involved.

Sample preparation

Finely ground CoSb₃ was blended with various weight percentages of carbon fiber (CF) and bulk samples prepared by spark plasma sintering (SPS) (Thermal Technology SPS Model 10–4) for 10 min at 500 K with 50 MPa pressure in vacuum. For comparison purposes, similar samples were prepared using graphene and graphene oxide. The CoSb₃ powder was purchased from Sigma-Aldrich, and the purity is 99.9% based on trace metal analysis with particle size being 177 microns. The bulk samples had 20 mm diameter and 1.5 mm thickness and were subsequently cut into rectangular bars and circular discs for electronic transport measurement using a cutting machine (Struers Accutom-50). Carbon fiber additions in the CoSb₃ samples are denoted by different weight percentages of carbon fiber ($x = 0.15, 0.35, 0.55, \text{ and } 0.95$ wt.%) and referred to as CoSb₃–CF_{*x*} throughout this paper. The corresponding volume fractions of carbon (based on a carbon fiber

density of 1.80 g/cm³) are 0.63, 1.47, 2.29, and 3.91 vol.%.

Sample characterization

Room temperature X-ray diffraction (XRD) was carried out using Bruker D8 Discover XRD and D5000 systems, both with Cu K α radiation. The samples were scanned in the 2θ range of 10–80° with a step of 0.02° and time per step = 1 s. The peaks due to Cu K β were attenuated by Ni filter (D5000). Structure files for CoSb₃, Sb, and graphite were obtained from the inorganic crystal structures database (ICSD) (<https://icsd.products.fiz-karlsruhe.de/>, entries 04–003-2101, 55,402, and 55,402, respectively) or from the Crystallographic Open Database (COD) (<https://crystallography.net>, entries 901–5513, 901–3415, and 900–8569, respectively). Rietveld refinement was applied using FULLPROF (www.ill.eu/sites/fullprof/index.html) called through MATCH! (www.crystalimpact.de). The surface morphology and microstructures were observed and studied using field emission scanning electron microscopy (FE-SEM, JSM-6490LV). Energy-dispersive X-ray spectroscopy (EDS) spectra were acquired with the same acquisition time, the same e-beam size, and the same microscopic condition as used in obtaining SEM images. The SEM specimens were prepared after mounted in PolyFast® using Struers CitoPress-20 equipment and polished with Struers Tegramin-20 water equipment. Image analysis was performed using IMAGEJ (<https://imagej.nih.gov/ij/download.html>). The electrical conductivity, Seebeck coefficient, and power factor were measured using an Ozawa RZ2001i at room temperature to 700 K under vacuum. Carrier concentration and mobility were measured using a 13 T automated low-temperature PPMS magnet system (Quantum Design International). Low-temperature resistivity was measured using the four-probe method. Thermal diffusivity (*D*) was measured using LINSEIS LFA 1000 (Linseis Messgeraete GmbH) under vacuum conditions, and the specific heat (*C_p*) capacity was measured using DSC-204F1 (Netzsch GmbH) under argon atmosphere with a flow rate of 50 ml/min. The sample density (*dd*) was calculated using the measured weight and dimensions. The thermal conductivity (κ) was calculated by $\kappa = D \times C_p \times dd$.

Results and discussion

Electronic structure properties

Electronic structure and density of states calculations were performed using density functional theory (DFT). We first performed optimization calculations to obtain an optimized crystal structure with a lattice parameter $a = 9.085 \text{ \AA}$ with the $Im\bar{3}$ cubic space group (No. 204). The resulting lattice, as shown in Fig. 1(a–c), closely matches those described in Schmidt [27] with $a = 9.04 \text{ \AA}$, giving an overestimated difference of 0.5%, in agreement with previous ab initio calculations [28]. The enthalpy of formation was -0.21 eV/atom which is slightly more negative than the -0.1 to -0.2 eV range of experimental

values reported in the literature [29]. A U value of 2.5 eV was used for Co.

The results for the band structures and density of states are shown in Fig. 1d and e. These closely match those described in Yang [30]. Band structure calculation results using the primitive cell shown in Fig. 1(b) of the pure CoSb_3 structure with the K-path in the Brillion zone of $\Gamma \rightarrow H \rightarrow N \rightarrow P \rightarrow \Gamma \rightarrow N$ (Fig. 1c) show the characteristics of a small-gap semiconductor. The semiconductor has a direct band gap of 0.224 eV that matches the value previously reported by Sofo [31]. Figure 1(e) shows the contributions of carriers from s , p , and d orbitals with the major contributor of the highest occupied molecular orbital (HOMO) being the p and d orbital electrons. The origin of these p and d orbitals is the Sb and Co atoms, respectively. Although Sb p vs Co d overall

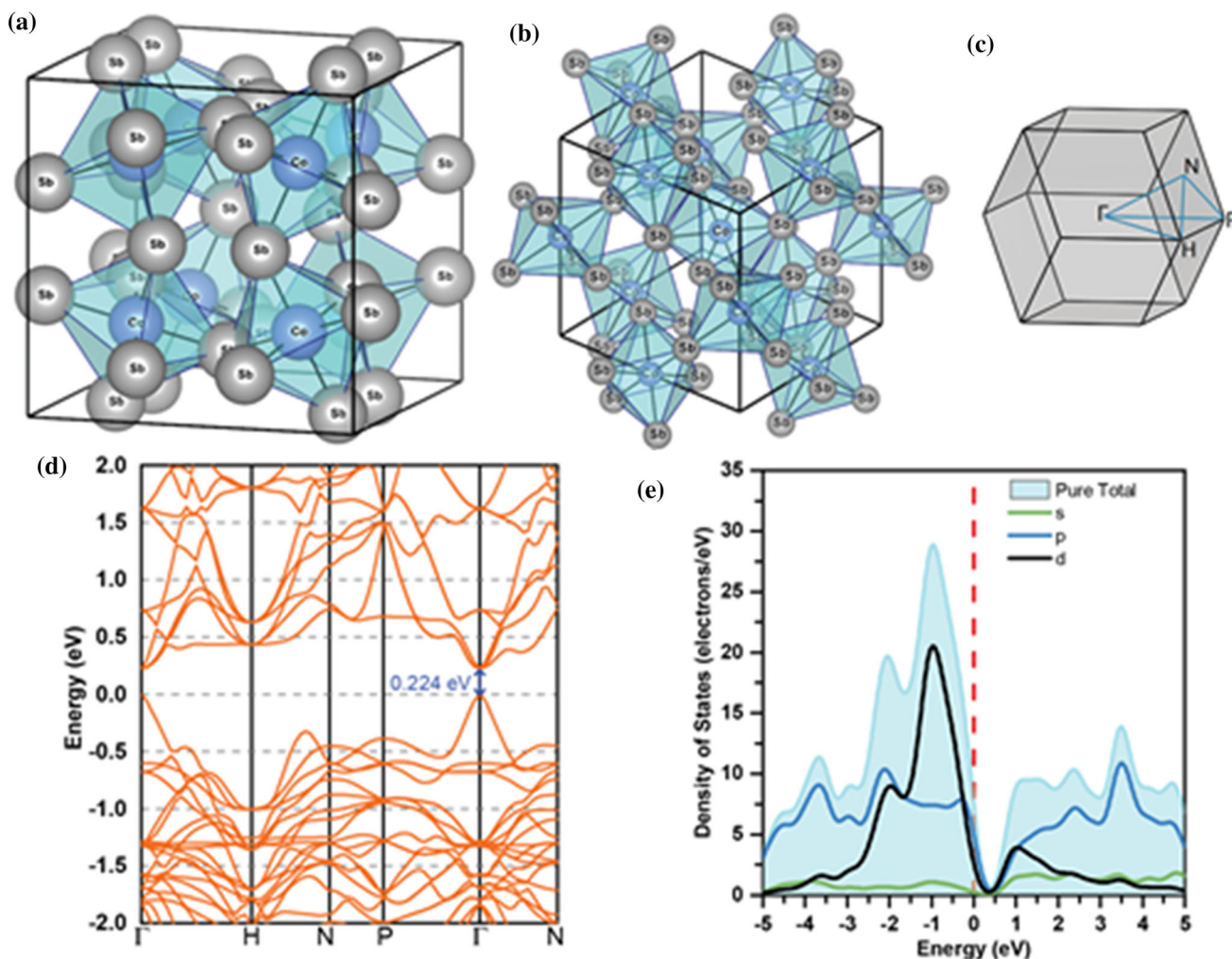


Figure 1 a Crystal structure of CoSb_3 unit cell, b primitive cell, c Brillouin zone of the primitive cell, d first-principles band structure calculation of pure CoSb_3 where the zero-energy point represents the Fermi level, e contributions of electrons from different orbitals.

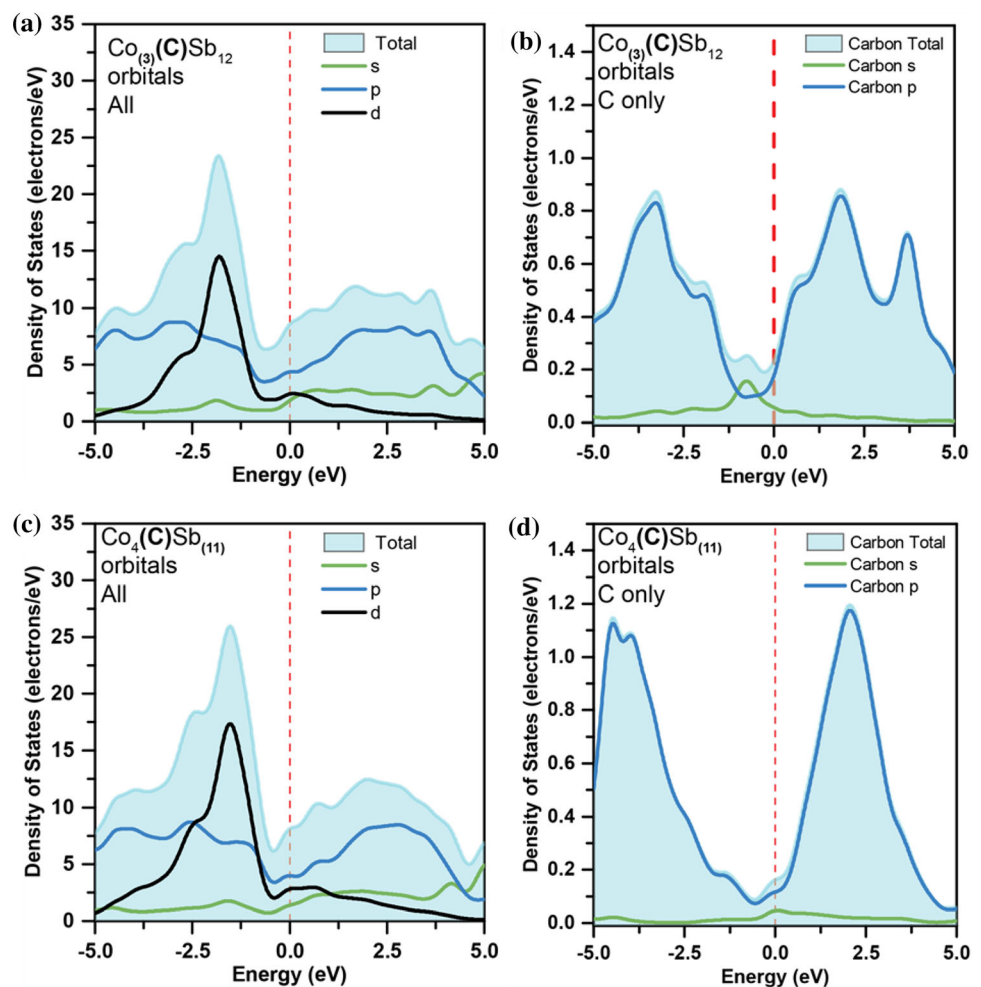
contributions are similar, it must be noted that there is 3 vs 1 population ratio and, as such, per atom the Co d orbital contribution to the HOMO is much higher.

Previous studies have concluded that CoSb_3 can be doped to become either n or p type [32, 33] depending on whether electron or hole dopants are used. Three scenarios have been taken into account for our calculations to simulate the possible impact of carbon in the CoSb_3 lattice. These include the replacement of either the Sb or Co ions with carbon atoms within the primitive CoSb_3 crystal structure (to simulate the substitutional states), the removal of the Co or Sb ions from within the crystal structure (to simulate defect states), and finally the insertion of one, two, and three carbons within the crystal structure (to simulate the interstitial states).

In our calculated results, we observe that in the C–Co substitutional state (Fig. 2a, b) there is a slight peak in the HOMO from the s orbital contributions

from the carbon atom and hence there is a similar contribution to the Fermi level between the s and d orbitals. Surprisingly, there is an overall increase in the p and d orbital contributions which is likely due to the result of the delocalization of the p orbitals from the d orbitals of the Co ions although it is of interest to note that d orbitals are also delocalized. This delocalization of d orbitals is likely attributed to the broken symmetry between the Sb and Co ions where d orbitals are partially delocalized from the Co. In the Sb substitutional state (Fig. 2c, d), we observe that there is a similar increase in the p and d orbital contributions although there is no s orbital HOMO peak. As such, the contribution to the Fermi level for d orbitals is much greater than the s orbital, but similarly, because of the broken symmetry, there is also a delocalization of the p orbitals from the Sb. However, in all cases, there is an overall increase in the total contribution at the Fermi energy.

Figure 2 Partial density of states for doped CoSb_3 in which carbon substitutionally dopes Co **a** and Sb **c** and the respective **b** and **d** partial density of states for their carbon contribution.



The calculated enthalpies of formation for the various configurations are listed in Table 1. Note that the formation of an interstitial solid solution of carbon at the $(1, \frac{1}{2}, \frac{1}{2})$ site, or the substitution of Sb with a carbon, is associated with a very small positive enthalpy. Stability depends, however, on the Gibbs free energy of formation, not enthalpy change. The effect of entropy and temperature must be considered via the relationship $\Delta G = \Delta H - T \cdot \Delta S$. In general, the introduction of defects increases disorder and entropy, so ΔS is positive for their formation. Therefore, the effect of a slightly positive ΔH can be negated at a sufficiently high temperature by the $-T \cdot \Delta S$ contribution. In this scenario, a dilute solution of carbon in the CoSb_3 lattice is feasible at some suitably elevated temperature.

Atoms are removed from the position as shown in Fig. 3c for Co and Fig. 3d for Sb. In both the Co defect states (Fig. 3a, there is a higher p orbital contribution for HOMO orbitals, due to the fact that p orbitals were previously localized by Co in the pure CoSb_3 . Hence, further enhancement of p orbital contributions can be observed since Sb d orbitals do not contribute to HOMO orbitals. In the Sb defect state, this is reversed and there is a comparatively higher d orbital HOMO contribution observed because of the delocalized d orbitals which were previously localized in pure CoSb_3 . The lowering of p orbital contribution is expected since the majority of the contribution comes from Sb. The changes in the orbitals are consistent with p - d hybridization between the p orbital of the Sb and d orbitals of the Co. In both cases, there is an overall increase in total contribution at the Fermi

energy. However, the defect doping states show a dominant p conduction of electrons.

The interstitial carbon states show an overall increase in the p orbital contribution of the HOMO which is due to the carbon p orbital contributions. Up to three carbon atoms are inserted into the lattice at three different positions in Fig. 4a where these are indicated as C1, C2, and C3. (The numerals indicate the total number of carbon atoms.) Our results show that the p orbital contribution increases with an increasing amount of carbon atoms (Fig. 4b–d). This carbon p orbital contribution is in addition to the Sb p orbital contributions to the HOMO (Fig. 4c. However, all interstitially doped orbitals show hole-like properties in their density of states Fig. 4b–d). As the number of carbon atoms increases, the contribution, per carbon atom, is decreasing (Fig. 5a). Finally, placing a carbon atom in a ‘rattler’ site is unfavorable. Similar trends emerge for all three cases: interstitial, substitutional, and defect doping—all increase the total density of states at the Fermi energy which can explain why there is an overall increase in the conductivity as all forms of defect will contribute to the overall increase in conductivity.

Structural and morphology characterization

The powder XRD patterns (Fig. 6) of all the samples indicate that the major peaks are from the polycrystalline skutterudite structure of CoSb_3 . There are also peaks for Sb in all of the samples to which CF was added. In some cases, a 002 graphite peak was also evident. Note, however, that the small amount (< 1 wt.%) of carbon deliberately added would not be

Table 1 Enthalpies of formation and relaxed lattice parameters from the DFT calculations. These calculations were performed with CASTEP and began with P1 symmetry on the primitive cell of the CoSb_3 structure. Enthalpies of formation are relative to the pure solid

Phase	Description	ΔH , eV/atom	a_0 , Å
$\text{Co}_8\text{Sb}_{24}$	Standard state	- 0.21	7.87
$\text{Co}_8\text{Sb}_{23}$	Sb deficient	- 0.05	7.82
$\text{Co}_7\text{Sb}_{24}$	Co deficient	- 0.084	7.87
$\text{Co}_7\text{Sb}_{24}\text{C}$	C on Co site	0.18	7.96
$\text{Co}_8\text{Sb}_{23}\text{C}$	C on Sb site	0.04	7.78
$\text{Co}_8\text{Sb}_{24}\text{C}$	Interstitial C at $(0, \frac{1}{2}, \frac{1}{2})$	0.05	7.91
$\text{Co}_8\text{Sb}_{24}\text{C}_3$	Interstitial C at $(0, 0, 0)$	0.18	7.89
$\text{Co}_8\text{Sb}_{24}\text{C}_3$	Interstitial C at $(0, \frac{1}{2}, \frac{1}{2})$, $(\frac{1}{2}, 0, \frac{1}{2})$ and $(\frac{1}{2}, \frac{1}{2}, 0)$	0.52	8.00

elements in their standard crystalline state at 0 K. The calculated enthalpy of formation of pure CoSb_3 is close to the $- 0.09$ to $- 0.16$ eV per atom reported from experiments [29]

Figure 3 Density of states for defects state (voids) doped CoSb_3 in which a void exists in the Co **a** and c and Sb **b** and **d** position.

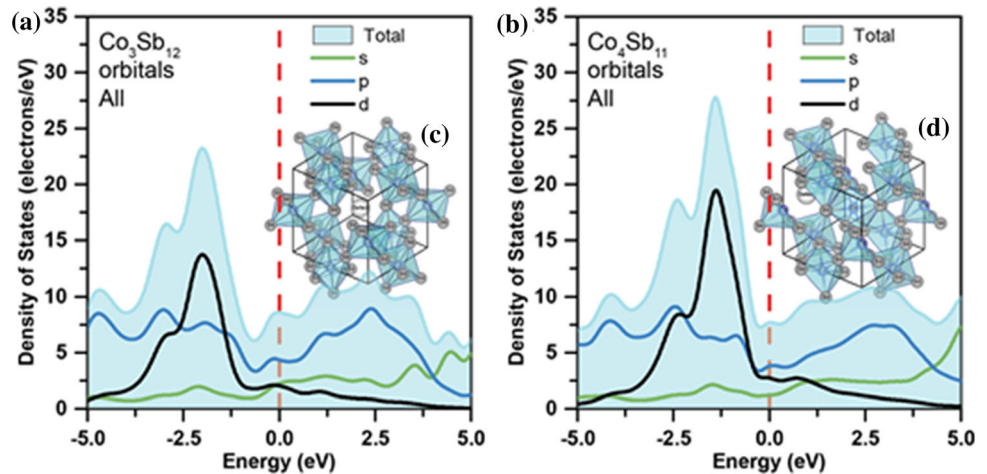
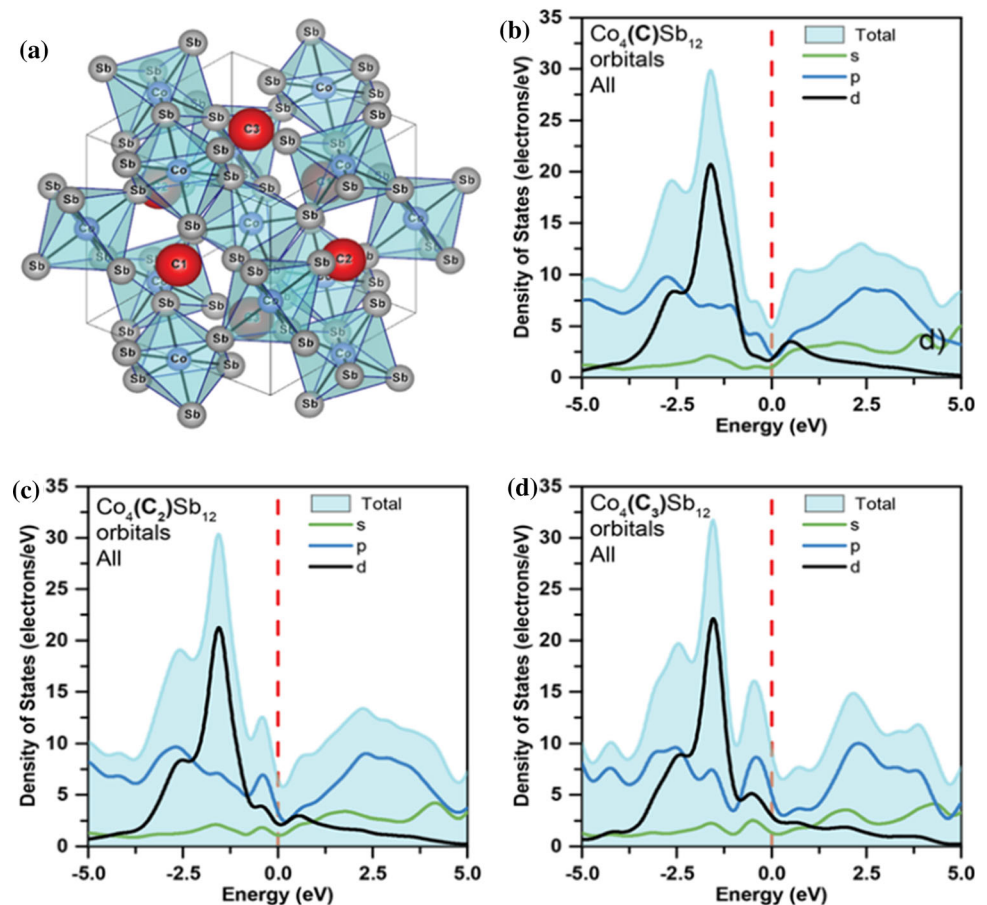


Figure 4 C1, C2, and C3 in **a** show the positions of the interstitial carbon doping. Density of states of interstitially doped CoSb_3 for **b** C1, **c** C2, and **d** C3 carbon ions.



detectable by XRD under the present conditions even if all of it was perfectly graphitized (an observation also made by Feng et al.[23]). We concluded, like Liu et al. [34] did, that the peak for graphite in samples made by SPS was spurious and due to residual graphite foil being present from the SPS synthesis. The results of the Rietveld analyses are provided in

Table 2. (The region containing the spurious 002 graphite peak was masked off in these refinements.) It is clear that (i) including CF up to 0.95 wt.% does not cause any significant change in lattice parameters of the CoSb_3 and (ii) the CF-containing samples contained a consistent 20 ± 2 wt.% elemental Sb as a second phase.

Figure 5 Comparison of all doping scenarios changes in **a** carbon, **b** Sb, **c** Co per each atom, and **d** their respective totals.

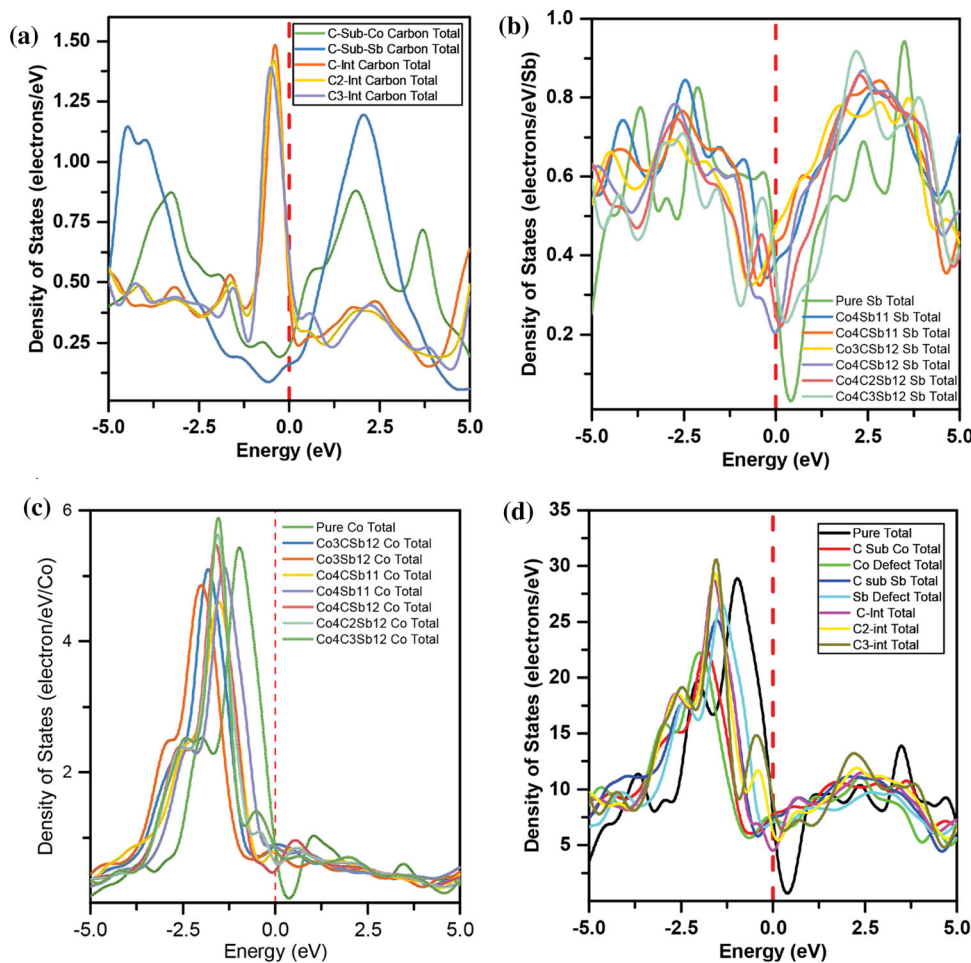


Figure 7 shows the SEM micrographs of polished sample surfaces (Fig. 7a–c) and cross section morphology (Fig. 7d–f) for the CoSb_3 polycrystalline samples with and without carbon fiber addition. The carbon fibers become quite prominent as the carbon concentration increases from $x = 0.15$ to 0.95 wt.%. The predicted volume fraction of carbon fiber in the 0.55 and 0.95 wt.% C samples is 2.3% and 3.9%, respectively (based on a CF density of 1.80 g/cm^3), while image analysis of the respective polished sections indicated values between 2 and 4%. Figure 8 shows the EDS mapping of the samples and confirms the presence of the CF but not of second phase Sb. We speculate that the Sb precipitates are below the resolution of the map. Raman measurements showed that the CF was slightly more graphitic after incorporation into the CoSb_3 matrix (Fig. 9). The experimental volume fractions and Raman spectra indicate that most of the CF passes unchanged through the SPS process. These results show that very little carbon is transferred from the CF into solution in the

CoSb_3 during processing. Therefore, it is not necessary that large amounts of carbon needed to have entered the CoSb_3 lattice in order to cause changes to the electronic structure.

All the samples are found to be densely aggregated, with little porosity. This is due to the relatively high temperature and pressure, and long times, used in the SPS processing. The grain sizes are about $5 \mu\text{m}$ or less. Energy-dispersive spectroscopy (EDS) performed on the $x = 0.55$ wt.% C sample is presented in Fig. 10 and confirms the identity of the microstructural constituents. By using the reported errors in the EDS, the ratio of Sb/Co was estimated to be in the range of 2.9 to 3.2, i.e., the sample should be mostly CoSb_3 .

Electrical and thermal properties

In Fig. 11, electrical conductivity *vs.* temperature is shown for different samples over a range of temperatures. The electrical conductivity increases by a

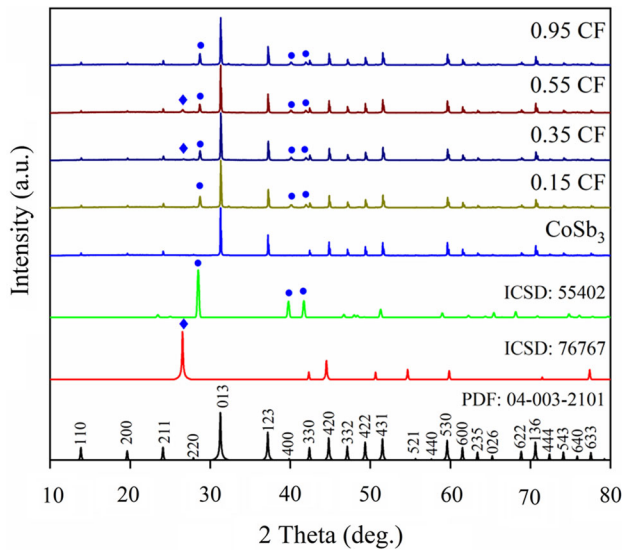


Figure 6 Room temperature X-ray diffraction patterns of the samples match with CoSb₃ (PDF number 04–003-2101), hexagonal structured carbon (ICSD collection code 76,767), and, in the samples with carbon fiber, trigonal structured antimony (ICSD collection code 55,402). CoSb₃ samples with a content of carbon fiber are named as CoSb₃-*x* wt% CF (*x* = 0, 0.15, 0.35, 0.55, and 0.95 wt.% carbon fiber).

factor of about three with increasing carbon fiber addition up to 0.35 wt.% C, but the effect saturates for greater additions. For the pure CoSb₃, the electrical conductivity rose from 271 S.cm⁻¹ at 330 K to 355 S.cm⁻¹ between 300 and 700 K, whereas the highest value (CoSb₃-CF0.35) reaches 1189 S.cm⁻¹ at 330 K and goes down to 973 S.cm⁻¹ at 700 K. Importantly, however, the trends depicted for pure CoSb₃ (*x* = 0) and the CoSb₃-CF*x* are qualitatively different: While a monotonic increase is observed in pure CoSb₃ from room temperature to 700 K, a noticeable drop occurs for the CoSb₃-CF*x* composites. These facts have important implications—the pure CoSb₃ is behaving as semiconductor (as it should), but the CoSb₃-

CF*x* composites are performing with a degree of metal-like behavior.

The enhancement of electrical conductivity in the CoSb₃-CF*x* composites is accompanied by a significant reduction in Seebeck coefficient (Fig. 11d). For example, the Seebeck value is only 65 μVK⁻¹ for CoSb₃-CF0.35 at 700 K as compared to 163 μVK⁻¹ at 700 K for pure CoSb₃. All the samples remain *p* type, as expected from their content of elemental Sb [34]. Although the direction of the change (the reduction in Seebeck coefficient) is consistent with the measured increase in carrier density, it is evident that some additional effect is operating so that the Seebeck coefficients of the CF-containing samples are reduced to about the same values as each other, to within statistical error.

Power factor (PF) = $S^2\sigma$ is represented in Fig. 12 as a function of temperature for CoSb₃-CF*x* composites and compared with pure CoSb₃. While carbon fiber additions significantly increased electrical conductivity, the Seebeck coefficients dropped below that of pure CoSb₃. Since Seebeck values are squared and multiplied with σ to obtain power factor, it can be appreciated that Seebeck values dominate over σ . For this reason, all the samples showed reduced power factor as compared to pure CoSb₃.

Thermal diffusivity (TD), specific heat capacity (C_p), and density (ρ) are the basic thermal property components which may be combined via $k = TD \times C_p \times \rho$ to yield thermal conductivity (k). The thermal conductivity arises from two contributions, the electronic thermal conductivity (K_e) and the phonon thermal conductivity (K_{ph}); therefore, total thermal conductivity is $K = K_e + K_{ph}$ [12]. It should be noted that the overall thermal conductivity is dominated numerically by phonon thermal conductivity which means that phonon vibration in the

Table 2 Results of rietveld refinement on a mixed CoSb₃ plus Sb microstructures

Wt.% carbon added as carbon fiber	Lattice parameter for CoSb ₃	Wt.% of Sb on surface from rietveld analysis	Weighted Bragg R factor	χ^2
0.00	9.0355 ± 0.0008	0	12.6	4.3
0.15	9.0363 ± 0.0005	22.5 ± 0.3	12.3	5.5
0.35	9.0363 ± 0.0005	18.1 ± 0.3	11.2	4.6
0.55	9.0356 ± 0.0003	20.1 ± 0.3	14.4	5.5
0.95	9.0361 ± 0.0003	20.4 ± 0.2	11.4	5.1

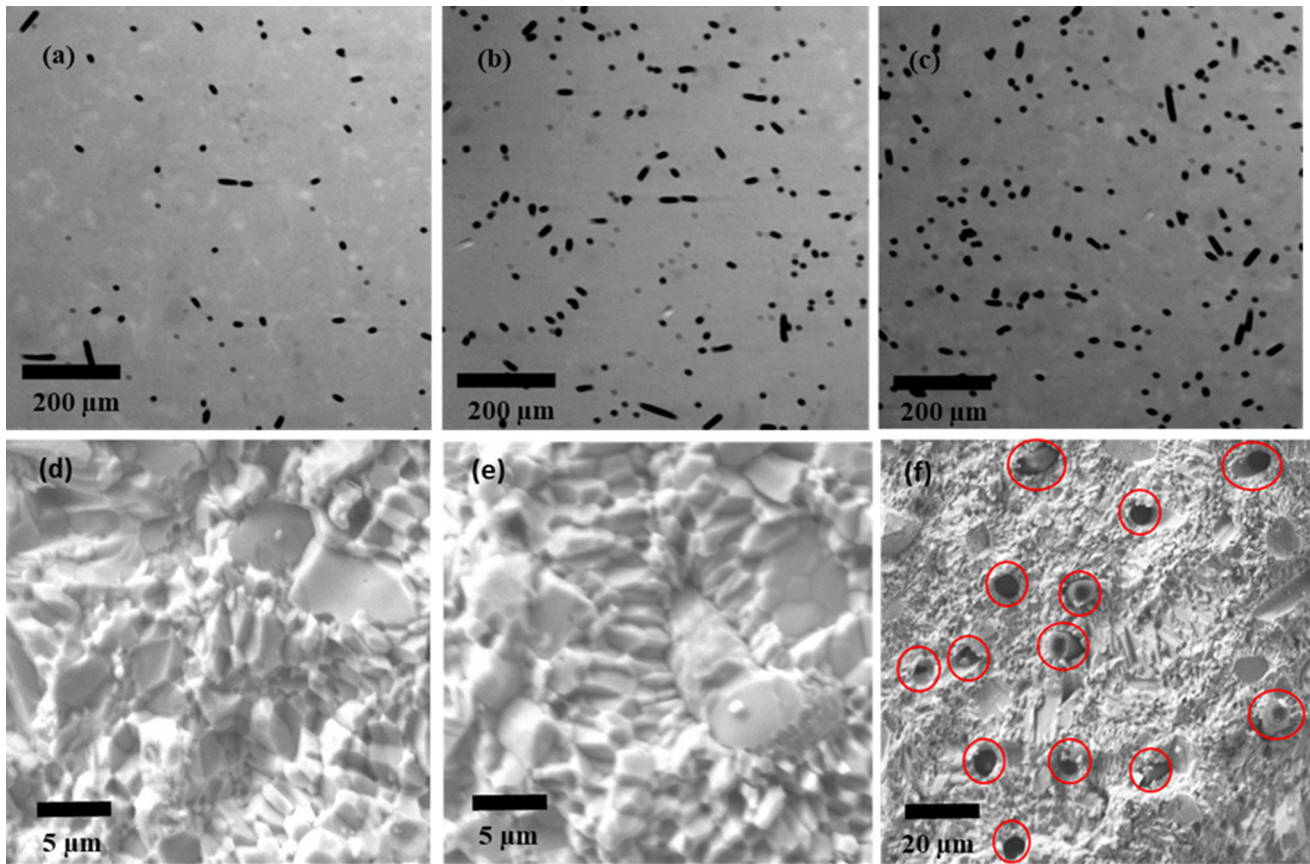


Figure 7 SE-SEM image of surface and cross-sectional morphology of CoSb_3 samples with nominal compositions of $\text{CoSb}_3\text{-CF}_x$ **a** and **d** $x = 0.15$ wt.%, **b** and **e** $x = 0.35$ wt.%, and

c and **f** $x = 0.55$ wt.%. Black dots in panels **a**, **b**, and **c** are carbon fiber on the surface. Red circles in panel **f** indicate carbon fibers found in the cross section.

lattice contributes to heat propagation more than electronic heat propagation at high temperature.

Measured thermal conductivity for the $\text{CoSb}_3\text{-CF}_x$ samples is shown in Fig. 13 as a function of temperature. The carrier component k_c (Fig. 13b) has been estimated using the Wiedemann–Franz law ($K_e = L \cdot \sigma \cdot T$, where L is a constant known as the Lorenz number [35]) and phonon thermal conductivity k_{ph} (Fig. 13c) found by difference. In this work, L is calculated according to the equation $L = 1.5 + \exp[-|S|/116]$, where L is in $10^{-8} \text{W}\Omega \cdot \text{K}^{-2}$ and S is in $\mu\text{V} \cdot \text{K}^{-1}$ [36, 37]. The calculated results show that L varies in the range of $(1.7 - 2.2) \times 10^{-8} \text{W}\Omega \cdot \text{K}^{-2}$ with different types of CF addition and with the temperature increasing from 330 to 700 K. The $\text{CoSb}_3\text{-CF}_x$ samples show *increased* carrier thermal conductivity over a wide range of temperature in Fig. 13b as the amount of carbon fiber added is increased.

K_{ph} is also observed to be increasing with carbon fiber addition (Fig. 13c) which could be due to the presence of carbon fiber in between the grain boundaries acting as a bridge between crystal boundaries, thereby helping phonons to travel from one grain to another. Actually, since thermal conductivity of carbon fiber can be much greater (up to as high as $180 \text{W}\cdot\text{m}^{-1}\cdot\text{K}^{-1}$ [38] depending on degree of graphitization) than that of the pure CoSb_3 ($\sim 8 \text{W}\cdot\text{m}^{-1}\cdot\text{K}^{-1}$ at room temperature), some increase in the overall value of k for an engineering composite made of the two substances is not unexpected. In contrast, some previous experiments have shown that carbon fiber or graphene in between grains can *reduce* the lattice thermal conductivity due to lattice mismatch between grain and carbonaceous second phase, both in CoSb_3 [39] and in Cu_2Se [40, 41]. We will return to this difference in behavior in the Discussion.

Figure 8 SE-SEM image of the polished 0.95wt.% CF-incorporated CoSb₃ sample, showing CF-rich precipitates within the CoSb₃-rich matrix along with the corresponding EDS elemental mapping for Co, Sb, and C.

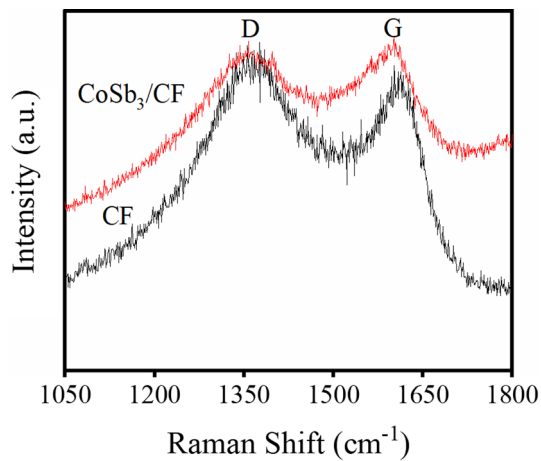
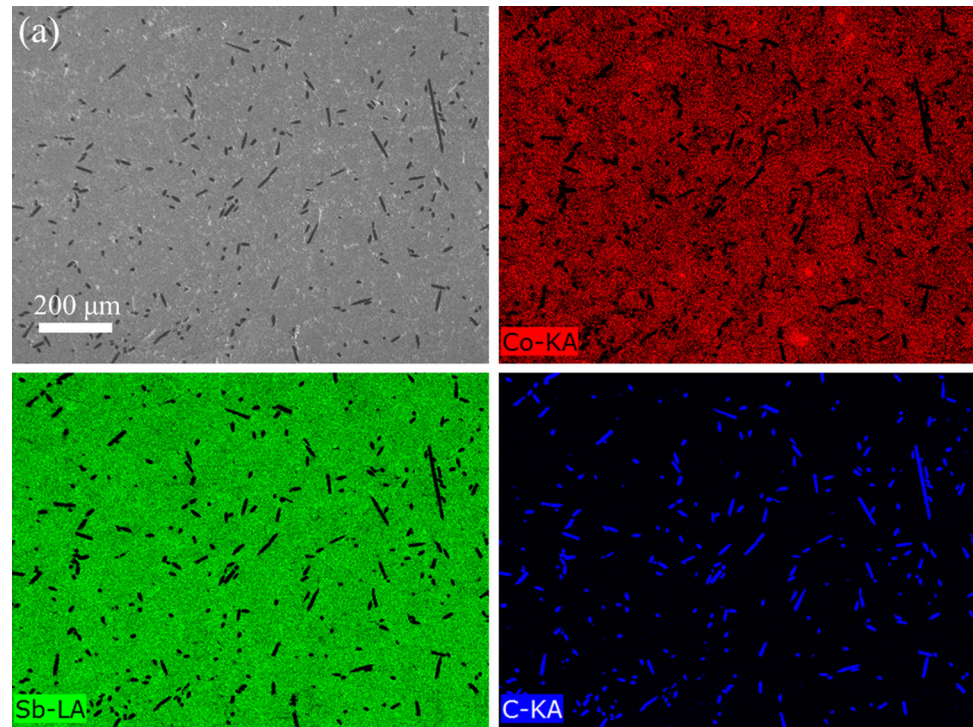


Figure 9 Raman spectra for carbon fiber before and after incorporation into sample.

Hall effect measurements

To further investigate the influence of carbon fiber addition on the transport properties of CoSb₃, we have measured the Hall effect of CoSb₃-CF_x samples at 300 K as shown in Fig. 14. Essentially, the Hall effect coefficient is being measured for a microstructural composite of CoSb₃, Sb, and CF and it is not a simple matter to extract the values for the individual phases [42]. As such, the values reported here can be considered to be those of an ‘effective medium’

representing the composite. The Hall coefficient is given by $R_H = \rho_{xy}/B$, where B is the magnetic flux density and ρ_{xy} is the Hall resistivity. The carrier concentration is $p = -1/(R_H e)$, where e is the electron charge. For all carbon concentrations, the values of R_H are positive indicating dominant p -type conduction (as indeed expected from the positive Seebeck coefficients). It can also be observed that the carrier concentration increases significantly with CF addition. Figure 14(b) shows the effect of carbon content on Hall mobility at 300 and 340 K, respectively. The Hall mobility follows the formula $\mu_H = R_H^* \sigma$; σ is the in-plane conductivity. Compared to pure CoSb₃ sample, the mobility decreases sharply with the initial addition of carbon. A further increase in carbon concentration results in a slight increment with minimal rate of change after $x = 0.35$ wt.%.

Discussion

Origin of enhanced electrical and thermal conductivity

Although the percolation of randomly packed conductive spheres occurs at a volume fraction of about 18% [43], it is a surprising fact that percolation of random dispersions of conducting fibers, or other

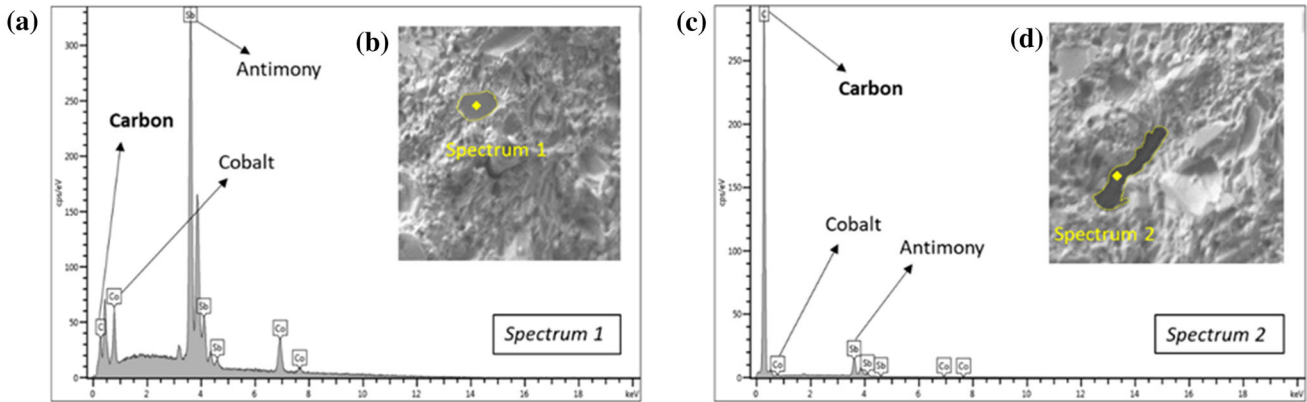
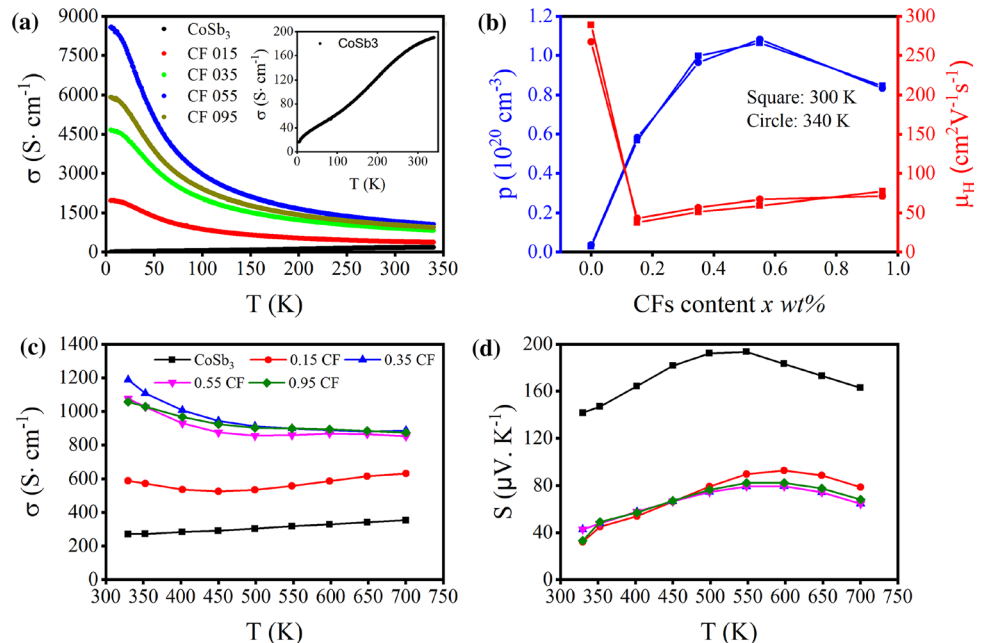


Figure 10 a Energy-dispersive X-ray spectroscopy (EDS) spectrum of the selected region of panel b and c, EDS spectrum of selected region of panel d. Both the Figures in b and d are CoSb₃-CF0.55 wt.%.

Figure 11 Temperature dependence of electrical transport properties of pure CoSb₃ and CF-incorporated CoSb₃ samples (CoSb₃-xwt% CF (x = 0, 0.15, 0.35, 0.55, and 0.95wt.% carbon fiber). a Low-temperature electrical conductivity (σ), b carrier concentration and carrier mobility, c high-temperature electrical conductivity (σ), d Seebeck coefficient (S) as a function of temperature.



reinforcements with very long aspect ratio, can occur in composite materials at as low as 0.5 vol.% [44–46]. The mechanism of conduction in such composites includes both direct electrical pathways and a network of tunnel junctions. This low threshold is well within the range of volume fractions of carbon fiber investigated in the present work. Accordingly, it is worth considering whether the present change in properties could be explained on the basis of electrical percolation through an engineering composite. Typical values for the electrical conductivity of industrial carbon fibers are of the order 20 to 1000 S.cm⁻¹. The spread is probably due to a variable degree of graphitization. This is of a similar order to the intrinsic properties of the CoSb₃ matrix anyway,

so percolation of CF is not likely to change the composite conductivity much. This may be verified by using the upper- and lower-bound mixture ‘rules’ for a percolating engineering composite [47]:

$$\sigma_c = V_{gr} \cdot \sigma_{gr} + (1 - V_{gr}) \cdot \sigma_{CoSb3} \tag{1}$$

or

$$\frac{1}{\sigma_c} = \frac{V_{gr}}{\sigma_{gr}} + \frac{(1 - V_{gr})}{\sigma_{CoSb3}} \tag{2}$$

where σ_c , σ_{gr} and σ_{CoSb3} are the electrical conductivities of composite, graphite, and CoSb₃, respectively, and V_{gr} is the volume fraction of graphite. If the conductivity of the pure CoSb₃ is taken as about 250 S.cm⁻¹, and that of the graphite is taken

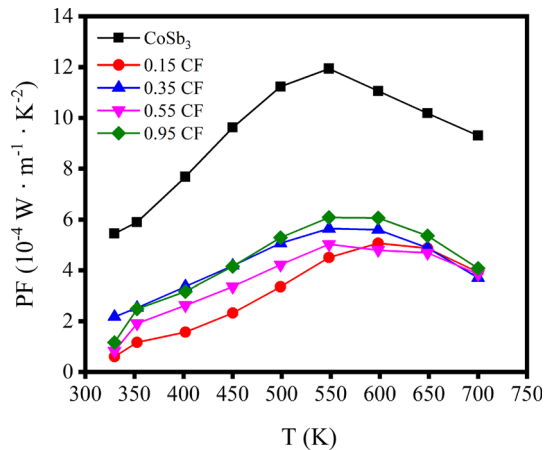


Figure 12 Temperature dependence of power factor of pure CoSb_3 and CF-incorporated CoSb_3 samples ($\text{CoSb}_{3-x}\text{wt}\%$ CF ($x = 0, 0.15, 0.35, 0.55,$ and $0.95\text{wt}\%$ carbon fiber).

(conservatively) as $1000 \text{ S}\cdot\text{cm}^{-1}$, then for the graphite volume fractions of 0.03, the electrical conductivity of the composite material should be between 255 and $270 \text{ S}\cdot\text{cm}^{-1}$. Actual values are nearly four times greater for this V_{gr} , so, clearly, percolation theory cannot explain the enhanced conductivity. Therefore, the changes in the present samples must be due to a change in the conductivity of the CoSb_3 matrix.

If a generic formula of the form $\text{CoSb}_{3-x}\text{C}_x$ is considered and if each carbon atom contributes one hole, then the observed carrier densities of the order of

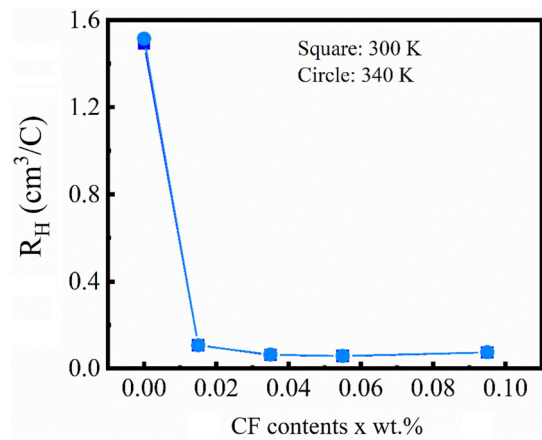
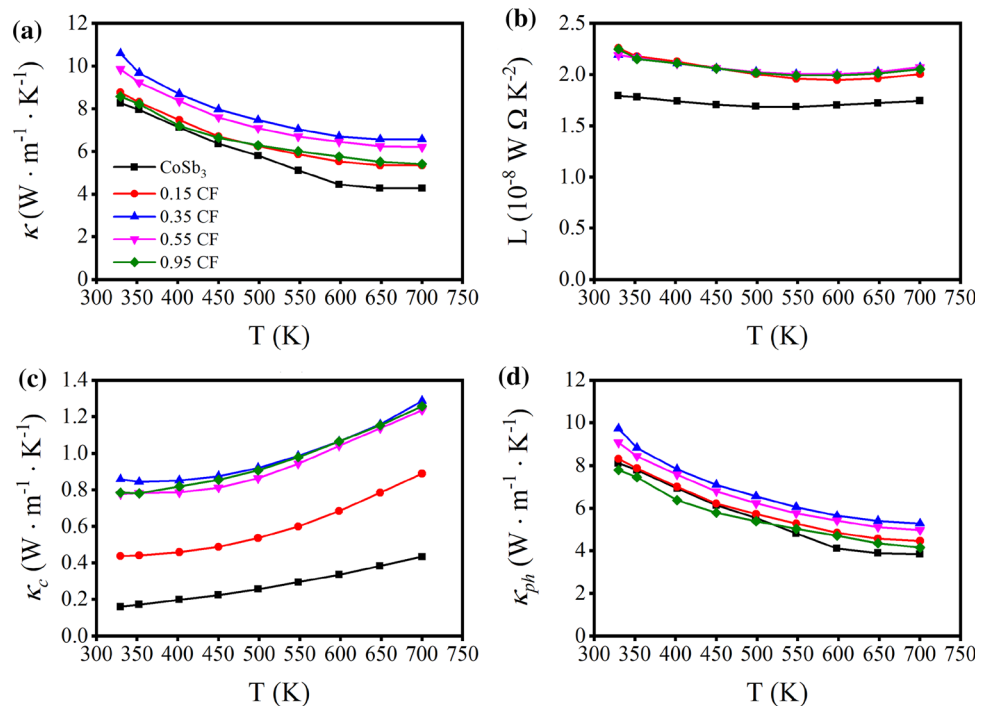


Figure 14 Hall effect at room temperature of pure and carbon-fiber-incorporated CoSb_3 samples.

$0.5 \times 10^{20} \text{ cm}^{-3}$ to $1 \times 10^{20} \text{ cm}^{-3}$ would be generated by carbon contents in the range of 0.5 to 1 at.%. This implies that sufficient carbon could have gone into solid solution to raise the carrier concentration. Note, however, that the effect on lattice parameter would still likely be too small to detect.

We have suggested that the increased carrier concentration may be due to the presence of carbon-containing defects within the CoSb_3 lattice. There is at least one other possibility that the carriers are generated in the defective structure lying at interface between the thermoelectric and the second-phase

Figure 13 Temperature dependence of thermal transport properties of $\text{CoSb}_{3-x}\text{wt}\%$ CF ($x = 0, 0.15, 0.35, 0.55,$ and 0.95) composites. **a** Total thermal conductivity (κ), **b** calculated Lorenz number (L), **c** carrier thermal conductivity (κ_c), and **d** phonon thermal conductivity κ_{ph} .



inclusions [48]. Further work is necessary to resolve the source of the increased conductivity.

Increased thermal conductivity

As mentioned earlier, the thermal conductivity in an electrically conductive solid may be broken into electronic and vibrational components. In the present composite system, high electrical conductivity is ensured by some change in the carrier characteristics due to carbon doping. This factor in turn provides a strong contribution to k_c . Scattering of phonons off carbonaceous inclusions, which has provided quite a reliable reduction in k_{ph} in other systems, including CoSb₃/graphene[39] and Cu₂Se/carbon[41], is simply overwhelmed in the present case by the electronic contribution to k . The overall result is that zT in this system is not improved by the CF additions (Fig. 15).

Conclusion

We have demonstrated a new approach for the fabrication of *p*-type CoSb₃-based composite material, whereby carbon fiber has been incorporated by the SPS method. The thermoelectric and electronic properties were investigated for carbon fiber contents of up to 0.55 wt.% (corresponding to 2.3 vol.% C). A threefold improvement in electrical conductivity over that of pure CoSb₃ was obtained when $x = 0.35$ wt.%C. This corresponds to ~ 1.5 vol.% carbon fiber.

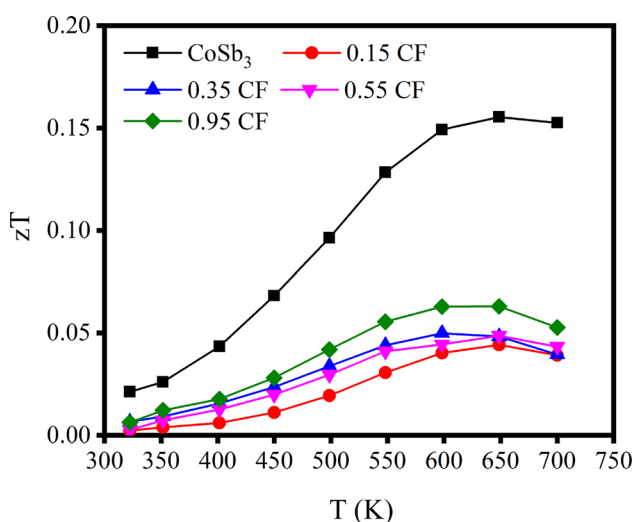


Figure 15 Temperature dependence of figure of merit (zT) of pure CoSb₃ and CF-incorporated CoSb₃ samples (CoSb₃- x wt% CF ($x = 0, 0.15, 0.35, 0.55,$ and 0.95 wt.% carbon fiber).

Additions of carbon fiber greater than this were not more beneficial. We suggest that, under the specific processing conditions used, some doping of carbon into the CoSb₃ lattice occurs when CF is added to the starting mixture at about 1.5 vol.%. Larger amounts do not contribute more to electrical conductivity. Thermal conductivity is slightly raised by the addition of carbon fiber. This illustrates that heat conduction in this system is dominated by electronic effects in the CoSb₃ matrix and that any increased scattering of phonons by the carbon fibers only has a secondary effect on thermal conductivity in these samples. Future work on this system must therefore necessarily concentrate on lowering thermal conductivity in order to restore the zT values, for example by including ‘rattler’ atoms within the CoSb₃ lattice.

Acknowledgements

Higher degree research of Ridwone Hossain was partially supported by a university faculty scholarship. This work was partially supported by the Australian Research Council (ARC) through Discovery Projects DP 130102956 (X.W.), DP 180100645 (M.C.), an ARC Professorial Future Fellowship project (FT 130100778, X.W.) and a Linkage Infrastructure Equipment and Facilities (LIEF) grant (LE 120100069, X.W.). The authors also acknowledge the use of the JEOL JSM 6490LV SEM funded by the Australian Research Council (ARC)—Linkage, Infrastructure, Equipment and Facilities (LIEF) located at the UOW Electron Microscopy Centre.

Declarations

Conflict of interest The authors declared that there is no conflict of interest.

References

- [1] Champier D (2017) Thermoelectric generators: A review of applications. *Energy Conv Manag* 140:167–181
- [2] Zhao D, Tan G (2014) A review of thermoelectric cooling: materials, modeling and applications. *Appl Thermal Eng* 66(1–2):15–24
- [3] Elsheikh MH, Shnawah DA, Sabri MFM, Said SBM, Hassan MH, Bashir MBA, Mohamad M (2014) A review on

- thermoelectric renewable energy: Principle parameters that affect their performance. *Renew Sust Energy Rev* 30:337–355
- [4] Liu W, Jie Q, Kim HS, Ren Z (2015) Current progress and future challenges in thermoelectric power generation: from materials to devices. *Acta Mater* 87:357–376
- [5] Miyazaki Y, Saito Y, Hayashi K, Yubuta K, Kajitani T (2011) Preparation and thermoelectric properties of a chimney-ladder (Mn_{1-x}Fex) Si γ ($\gamma \sim 1.7$) solid solution. *Jpn J Appl Phys* 50 (3R):035804
- [6] Özdemir AE, Köysal Y, Özbaş E, Atalay T (2015) The experimental design of solar heating thermoelectric generator with wind cooling chimney. *Energy Conv Manag* 98:127–133
- [7] Wang Y, Dai C, Wang S (2013) Theoretical analysis of a thermoelectric generator using exhaust gas of vehicles as heat source. *Appl Energy* 112:1171–1180
- [8] Espinosa N, Lazard M, Aixala L, Scherrer H (2010) Modeling a thermoelectric generator applied to diesel automotive heat recovery. *J Electron Mater* 39(9):1446–1455
- [9] Carlson EJ, Strunz K, Otis BP (2010) A 20 mV input boost converter with efficient digital control for thermoelectric energy harvesting. *IEEE J Solid-State Circuits* 45(4):741–750
- [10] Dolz V, Novella R, García A, Sánchez J (2012) HD diesel engine equipped with a bottoming rankine cycle as a waste heat recovery system. part 1: study and analysis of the waste heat energy. *Appl Thermal Eng* 36:269–278
- [11] Saidur R, Rezaei M, Muzammil WK, Hassan M, Paria S, Hasanuzzaman M (2012) Technologies to recover exhaust heat from internal combustion engines. *Renew Sustain Energy Rev* 16(8):5649–5659
- [12] Snyder GJ, Toberer ES (2008) Complex thermoelectric materials. *Nature Mater* 7:105–114. <https://doi.org/10.1038/nmat2090>
- [13] Dresselhaus MS, Chen G, Tang MY, Yang R, Lee H, Wang D, Ren Z, Fleurial JP, Gogna P (2007) New directions for low-dimensional thermoelectric materials. *Adv Mater* 19(8):1043–1053
- [14] Sootsman JR, Chung DY, Kanatzidis MG (2009) New and old concepts in thermoelectric materials. *Angew Chem Int Ed* 48(46):8616–8639
- [15] Rull-Bravo M, Moure A, Fernandez J, Martin-Gonzalez M (2015) Skutterudites as thermoelectric materials: revisited. *RSC Adv* 5(52):41653–41667
- [16] Gainza J, Serrano-Sánchez F, Rodrigues JE, Prado-Gonjal J, Nemes NM, Biskup N, Alonso JA (2020) Unveiling the correlation between the crystalline structure of M-filled CoSb₃ (M= Y, K, Sr) skutterudites and their thermoelectric transport properties. *Adv Func Mater* 30(36):2001651
- [17] Shi X, Yang J, Wu L, Salvador JR, Zhang C, Villaire WL, Haddad D, Yang J, Zhu Y, Li Q (2015) Band structure engineering and thermoelectric properties of charge-compensated filled skutterudites. *Sci Rep* 5:14641. <https://doi.org/10.1038/srep14641>
- [18] Choi S, Kurosaki K, Harnwungmoung A, Miyazaki Y, Ohishi Y, Muta H, Yamanaka S (2015) Enhancement of thermoelectric properties of CoSb₃ skutterudite by addition of Ga and In. *Jpn J Appl Phys* 54 (11): 111801
- [19] Liu W-S, Zhang B-P, Zhao L-D, Li J-F (2008) Improvement of thermoelectric performance of CoSb_{3-x}Tex Skutterudite compounds by additional substitution of IVB-group elements for Sb. *Chem Mater* 20(24):7526–7531. <https://doi.org/10.1021/cm802367f>
- [20] Rogl G, Grytsiv A, Yubuta K, Puchegger S, Bauer E, Raju C, Mallik RC, Rogl P (2015) In-doped multifilled n-type skutterudites with ZT=1.8. *Acta Mater* 95:201–211. <https://doi.org/10.1016/j.actamat.2015.05.024>
- [21] Zhao W, Liu Z, Wei P, Zhang Q, Zhu W, Su X, Tang X, Yang J, Liu Y, Shi J (2017) Magnetoelectric interaction and transport behaviours in magnetic nanocomposite thermoelectric materials. *Nature Nanotech* 12(1):55
- [22] Zhao W, Liu Z, Sun Z, Zhang Q, Wei P, Mu X, Zhou H, Li C, Ma S, He D (2017) Superparamagnetic enhancement of thermoelectric performance. *Nature* 549(7671):247
- [23] Feng B, Xie J, Cao G, Zhua T, Zhao X (2013) Enhanced thermoelectric properties of p-type CoSb₃/graphene nanocomposite. *J Mater Chem A* 1:13111–13119
- [24] Clark SJ, Segall MD, Pickard CJ, Hasnip PJ, Probert MI, Refson K, Payne MC (2005) First principles methods using CASTEP. *Z Kristallographie-Crystalline Materials* 220 (5/6):567–570
- [25] Perdew JP, Burke K, Ernzerhof M (1996) Generalized gradient approximation made simple. *Phys Rev Lett* 77(18):3865–3868. <https://doi.org/10.1103/PhysRevLett.77.3865>
- [26] Shanno DF (1970) Conditioning of quasi-newton methods for function minimization. *Math Comput* 24(111):647–656. <https://doi.org/10.2307/2004840>
- [27] Schmidt T, Kliche G, Lutz H (1987) Structure refinement of skutterudite-type cobalt triantimonide, CoSb₃. *Acta Crystallogr C* 43(9):1678–1679
- [28] Guo R, Wang X, Huang B (2015) Thermal conductivity of skutterudite CoSb₃ from first principles: substitution and nanoengineering effects. *Sci Rep* 5:7806
- [29] Schlesinger ME (2013) Thermodynamic properties of solid binary antimonides. *Chem Rev* 113:8066–8092
- [30] Yang J, Zhang L, Liu Y, Chen C, Li J, Yu D, He J, Liu Z, Tian Y, Xu B (2013) Investigation of skutterudite

- Mg₃Co₄Sb₁₂: High pressure synthesis and thermoelectric properties. *J Appl Phys* 113 (11):113703
- [31] Sofo JO, Mahan GD (1998) Electronic structure of CoSb₃: A narrow-band-gap semiconductor. *Phys Rev B* 58(23):15620
- [32] Shi X, Yang J, Salvador JR, Chi M, Cho JY, Wang H, Bai S, Yang J, Zhang W, Chen L (2011) Multiple-filled skutterudites: high thermoelectric figure of merit through separately optimizing electrical and thermal transports. *J Amer Chem Soc* 133(20):7837–7846
- [33] Rogl G, Grytsiv A, Rogl P, Bauer E, Kerber M, Zehetbauer M, Puchegger S (2010) Multifilled nanocrystalline p-type didymium–Skutterudites with ZT > 1.2. *Intermetallics* 18 (12):2435–2444
- [34] Liu W-S, Zhang B-P, Li J-F, Zhao L-D (2007) Effects of Sb compensation on microstructure, thermoelectric properties and point defect of CoSb₃ compound. *J Phys D: Appl Phys* 40:6784–6790
- [35] Ashcroft NW, Mermin ND (1976) *Solid State Physics*. Harcourt College Publishers, New York, College Edition edn
- [36] Kim H-S, Gibbs ZM, Tang Y, Wang H, Snyder GJ (2015) Characterization of Lorenz number with Seebeck coefficient measurement. *APL Mater* 3 (4):041506
- [37] Mehta RJ, Zhang Y, Karthik C, Singh B, Siegel RW, Borca-Tasciuc T, Ramanath G (2012) A new class of doped nanobulk high-figure-of-merit thermoelectrics by scalable bottom-up assembly. *Nature Mater* 11(3):233
- [38] El-Hage Y, Hind S, Robitaille F (2018) Thermal conductivity of textile reinforcements for composites. *J Textiles Fibrous Mater* 1:1–12
- [39] Zong P, Hanus R, Dyll M, Tang Y, Liao J, Zhang Q, Snyder GJ, Chen L (2017) Skutterudite with graphene-modified grain-boundary complexion enhances zT enabling high-efficiency thermoelectric device. *Energy Environ Sci* 10:183–191
- [40] Islam SMKN, Cortie MB, Wang X (2020) Grape juice: an effective liquid additive for significant enhancement of thermoelectric performance in Cu₂Se. *J Mater Chem A* 88(33):16913–16919
- [41] Li M, Cortie DL, Liu J, Yu D, Islam SMKN, Zhao L, Mitchell DRG, Mole RA, Cortie MB, Dou S, Wang X (2018) Ultra-high thermoelectric performance in graphene incorporated Cu₂Se: role of mismatching phonon modes. *Nano Energy* 53:993–1002
- [42] Day TW, Zeier WG, Brown DR, Melot BC, Snyder GJ (2014) Determining conductivity and mobility values of individual components in multiphase composite Cu_{1.97}-Ag_{0.03}Se. *Appl Phys Lett* 105:172103
- [43] Powell MJ (1979) Site percolation in randomly packed spheres. *Phys Rev B* 20(10):4194–4198
- [44] Miyasaka K, Watanabe K, Jojima E, Aida H, Sumita M, Ishikawa K (1982) Electrical conductivity of carbon-polymer composites as a function of carbon content. *J Mater Sci* 17:1610–1616
- [45] Haghgoo M, Ansari R, Hassanzadeh-Aghdam MK, Nankali M (2019) Analytical formulation for electrical conductivity and percolation threshold of epoxy multiscale nanocomposites reinforced with chopped carbon fibers and wavy carbon nanotubes considering tunneling resistivity. *Composites Part A* 126:105616
- [46] Motaghi A, Hrymak A, Motlagh GH (2015) Electrical conductivity and percolation threshold of hybrid carbon/polymer composites. *J Appl Polymer Sci*. <https://doi.org/10.1002/A PP.41744>
- [47] Callister WD, Rethwisch DG (2014) *Materials Science and Engineering. An Introduction*. 9th Ed. edn. Wiley
- [48] Wu C-F, Wang H, Yan Q, Wei T-R, Li J-F (2017) Doping of thermoelectric PbSe with chemically inert secondary phase nanoparticles†. *J Mater Chem C* 5:10881. <https://doi.org/10.1039/c7tc03614k>

Publisher's Note Springer Nature remains neutral with regard to jurisdictional claims in published maps and institutional affiliations.